



Crack Monitoring Potential of Smart Graphene Nanoplatelet (GNP)-Doped Poly (methyl methacrylate) (PMMA) Spray-Coated Sensor Compared to Conventional Ultrasound in Simple Structures

D Sethy¹ · Sandeep Kumar S R¹ · K Balasubramaniam¹

Received: 24 February 2022 / Accepted: 13 August 2022 / Published online: 23 September 2022
© The Author(s), under exclusive licence to Springer Science+Business Media, LLC, part of Springer Nature 2022

Abstract

High piezoresistive smart nanocomposites strain sensors have attracted much attention because of their sensing ability to monitor structural integrity. Current nano-sensors have been successfully manufactured, but due to fabrication cost and inefficiency in multitasking, they are not in demand. This paper mainly focuses on the comparative study between advanced smart sensors called graphene nanoplatelets (GNP) and conventional ultrasound sensor in the context of SHM in stainless steel. Here, the electrical resistance of the smart GNP sensor with the propagation of crack growth shifts from its baseline with the application of spectrum loading, which is helpful in crack failure. The post-processing method by conventional ultrasound is only helpful after the post-failure but not during crack propagation, which can be replaced by the GNP-doped poly (methyl methacrylate) PMMA sensor. Stresses around the hole change their shape from circular to elliptic, which is explained with the help of 2D Extended Finite Element Method (XFEM) simulations and the crack opening mechanism by Abaqus 6.12. After 3* (1st spectrum loading), it was difficult to spot the crack location, which was monitored smartly with a graphene sensor. GNPs are highly sensitive to cyclic spectrum loading. Structural health monitoring (SHM) has been done by a graphene doped PMMA sensor having the highest gauge factor (GF) of 800Ω, that is 84. The electrical resistance's baseline shifting was found to increase with crack growth. The GNPs spray-coated nano-sensor helps in the early detection of crack propagation before failure. Hence, this can save the cost and life of structural components, which ultrasound sensor cannot do during crack growth.

Keywords Extended finite element method · Spectrum fatigue loading · Strain sensor · Ultrasonics · Graphene nanoplatelets · Scanning electron microscope

1 Introduction

SS304, the strongest alloy among all steel grades, has high corrosion resistance and vast application in aerospace, automotive, machine and industry. It has high tensile strength, shear modulus and melting point. So, in the aerospace industry, it is used in making actuators, fasteners and landing gear components. Sometimes these industries face high impact damages that are very difficult to inspect in advance with non-destructive techniques like conventional ultrasound by

the time of flight technique. The time of flight (ToF) method is usually used for post-processing non-destructive test (NDT) analysis, that is, after failure. This NDT approach sometimes doesn't promise an accurate result, which can be replaced with a smart graphene doped PMMA sensor that helps to monitor clearly by spray coating upon steel [1]. Graphene is a 2-dimensional crystalline allotrope of carbon that is sp² hybridized and densely packed in a honeycomb crystal lattice. GNPs are the genesis of various disruptive technologies spread across many industrial sectors. The unique properties of graphene, like good mechanical strength, surface area, flexibility, high thermal and electrical conductivity help graphene sense the environmental changes during structural health monitoring purposes [2]. Graphene aims to foster high-graded and quality-based smart technologies for intelligent sensing by implementing the industry 4.0

✉ D Sethy
debadatta6@gmail.com

¹ Center for Non-destructive Evaluation, Institute of Technology Madras, 600036 Chennai, India

approach [3]. Graphene nanomaterials, called functionalized materials, always come with a substrate for good stability and mechanical strength. Many studies on graphene nanomaterials have been conducted, with PMMA serving as the substrate for strain monitoring, gas sensors and thermal signature. Piezoresistive action by GNPs also was studied in smart nanocomposites to metal matrix composite [4]. Spray-coated sensors fabricated from GNPs had been studied in vast growth for the sensing purpose during mechanical dynamic and static loading, where the maximum gauge factor was 77 ± 1 [5]. GNPs have shown a promising concern for the industry for a few decades, where they have played a major role in flaw detection. SS304 always faces a serious concern in the aerospace industry during damage, and its inspection matters a lot for the risk of life. GNPs not only help in strain data acquisition in terms of electrical resistance but also help in improving thermal signature [6]. Graphene's surface-related work has focused on developing sensors for sensing mechanical damage. GNPs skin coated sensor in glass fibre composites (GFRP) has already identified defects. During uniaxial loading, the GNPs skin-coated sensor upon GFRP has already retained heat better than without coating [7]. In structural health monitoring, advanced sensors like lead-zirconium-titanate (PZT) have also played many roles, like mechanical strain monitoring and heat sensing capability. But these PZT sensors in the commercial form are available without purity. It always comes in donor dopants or acceptor dopants, which facilitates cation vacancies with domain wall motion in the material. Their cost of fabrication is a little complex and also costly. The work reported in the past either uses PZT sensors, metallic foil strain gauges or reduced forms of graphene with polymer functionalized groups. Those sensors are less sensitive with less gauge factor (GF). Those sensors may deteriorate over time and again undergo the making process with difficulty in fabrication and synthesis. At the same time, multipurpose smart work like improving thermal signature, piezoresistivity in mechanical deformation, and bio-sensing have not been studied. In the literature and in industrial applications, real-time monitoring, stretchability, thermal conductivity, bio-sensing with cost constraints and complex fabrication have been reported. Smart skin-coated sensor networks by PZTs for aircraft health monitoring have been reported [8]. A proposed serpentine-based fractal island interconnected structure combined with the flexible printed circuit manufacturing process. The main objective here was to show the receiving and exciting performance of PZTs on network circuits in response to guided waves. Piezoelectric (PZT) elements and wires for structural health monitoring (SHM) were fabricated on a glass-fibre reinforced plate. PZT is arranged along the row and column method, interconnected with copper wire to detect structural

impact and damage regions of GFRP [9]. Advanced carbon allotrope-based graphene nanoplatelet strain sensors have piqued researchers' interest in piezoresistive action due to their low fabrication cost and high sensitivity. Work has also been studied to improve electrical and mechanical properties by a blending approach with graphene nanosheets. With an increase in the percentage of graphene, the electrical properties of polymer nanocomposites have shown a significant improvement after reaching a percolation threshold of 3.33 wt % [10]. Due to an increase in graphene wt. load level to 20%, the nanoparticle-filled epoxy composite increased thermal conductivity by 28 fold. Much work has been done with hybrid graphene aerogels for increasing thermal energy storage by 1.8 wt % GNPs. Polyethylene glycol (PEG) has always been a suitable agent in graphene aerogel due to its high latent heat storage capacity. The interfacial adhesion between graphite and the polymer matrix has also remarkably improved thermal conductivity. This, as a result, also increased the mechanical properties [11].

Some low-cost materials like PVDF have also been found to be superior by doping in graphene to improve the tensile strength and thermal conductivity [12]. Thermal conductivity increased to 212 % by increasing 20 wt % of graphene. Another derived form of graphene-like nanosheets by doping into sulfonated polystyrene had shown a good thermal signature by incorporating GNP filler in a wavy pattern [13, 14]. Some 3D patterns of graphene structure doped with polyamide composites also had enhanced thermal conductivity [15]. A susceptible temperature sensor was also developed by doping monolayer graphene to PVDF-TrFE that examined low temperatures in the range of -200 °C and high temperatures (0–300 °C) [16]. Even some other sandwich techniques had been studied for developing thermal emitter substrate, but this had always been challenging to fabrication cost and reliability. GNP has not only proved itself a good candidate for thermal control but also has shown a promising result toward strain monitoring potential in structures [17–19]. An advanced strain sensor has been developed by diffusing graphene into natural rubber, where the gauge factor was achieved at 6.5 with 12 % strain and 46 with a strain of 3 % [20]. This natural rubber/pristine graphene strain sensor development showed profound interest in measuring bodily motion. Graphene also showed its excellent sensing ability in textile-based strain sensors [21]. Also, 3D printed strain gauges out from graphene have been able to predict strain in vehicles by wireless data transfer electronics. The piezoresistive action between sensor and tyre vibrations leads to strain development, increasing the resistance [22–26]. Much work has been done on improving graphene synthesis to increase sensitivity [27]. The modified hummer's method has helped improve the hydrophilic nature. These carbon-derived sensors have been considered

to be the next-generation gas sensor due to their good properties like mechanical strength, flexibility, high surface-to-volume ratio and large conductivity [28–31]. Many sensors out from graphene have always shown the best possibility for strain sensor candidates in structural components. These GNP sensors monitored crack growth in cyclic loading and showed the best performance in human motion detection [32–37]. High selectivity is required for multiple stimuli with cost-effective and facile fabrication methods with excellent uniformity. Multifunctional sensing ability and mechanical durability are in high demand. Especially integrated multifunctional sensors with feedback point-of-care therapy to construct a closed-loop system are significant in disease management. Spray-coated GNP-doped sensor has been implemented to overcome the existing problems like ineffectiveness, durability and cost of fabrication etc. It is durable and long-lasting with a cheap fabricating approach-based sensor that can be redone repeatedly. Others reported sensors in literature are of the reduced form of graphene and are of low sensitivity because of functionalized polymer that increases the resistance. The sensitivity of this sensor provides a multifunctional approach in the context of mechanical deformation, improving thermal signature and bio-sensing compatibility.

The goal of this study fulfilled in this article is to compare the sensitivity performance of the GNPs/PMMA sensor in crack growth monitoring during spectrum fatigue loading in SS304 against the post-processing conventional ultrasound NDT technique. A spray-coated GNPs/PMMA sensor has been fabricated on SS304 and was tested for health monitoring under spectrum loading. This GNPs sensor helped detect crack growth at an early stage of complete failure, which was compared against conventional ultrasound after crack growth. It is the best sensor for saving and analyzing structural failure. It has been proved in this article that GNPs doped PMMA sensors not only monitor crack growth but also could be a promising candidate for saving human lives during structural failures. This early crack growth detection cannot be monitored during crack propagation by conventional ultrasound sensor, which usually uses a post-processing approach after loss.

2 Fabrication and Experimental Set-up

As shown in Fig. 1, GNPs, PMMA, and Tetrahydrofuran (THF) were used to synthesize the GNPs/PMMA sensor. Here, GNPs (thickness < 2–4 nm; lateral size = 5 μm , were obtained generously from GRAPHENE LAB Ltd, London, UK) were doped inside PMMA (average MW ~ 120 000 g/mol, was purchased from Sigma-Aldrich) as filler for the fabrication of nanocomposite strain sensor. THF-AR has

been used as the solvent for dispersing GNPs and PMMA. First, as shown in Figs. 1a and 50 mg of GNPs are mixed with 75 ml of THF. Then it was set under an ultrasonicator for 24 h. Then, separately, 3 mg of PMMA was added to 75 ml of THF in a glass bottle vial and was set for sonication at a frequency of 135 kHz and at 80% power for under 24 h at a temperature of 35 $^{\circ}\text{C}$. Then both the solutions GNPs/THF and PMMA/THF were added and again set under sonication for 24 h. Then the solution was sprayed upon SS304 at an area of 30 mm \times 20 mm. Then it was set under curing at room temperature for three days to get dried up. Then wire leads were attached to the sensor and were studied for electrical change in terms of resistance with the Keithley source meter. Wire leads were connected with carbon conducting paste (Anders Products, MA02176). Instron-8801 was used to perform mechanical fatigue testing with a GNPs sensor spray-coated to SS304, as shown in Fig. 1b. Spectrum fatigue load with position control mode, as shown in Fig. 7, was tested upon a specimen coated with GNPs/PMMA sensor. With amplitude varying from 0.1 to 0.5 mm and slowly decreasing down to 0.1 mm from 0.4 mm by increasing the frequency from 3 times of 1st spectrum loading to 6 times of 1st spectrum loading, reaching 10 times, and finally at a failure load of 20 times of 1st spectrum loading. After and before testing, crack propagation and defects were studied under an optical macroscopy stereo zoom lens at a resolution of 1 mm. Then a post-processing technique was employed for SHM of SS304 by the time of flight (ToF) method in the RITEC pulser receiver with a 1 MHz longitudinal transducer, as shown in Fig. 1d.

3 Characterization

The GNP doped PMMA sensor was subjected to SEM (*INSPECT F-50*) to assess the morphology of the spray-coated sensors, as shown in Fig. 2. GNPs are flaky and palm-like flat structures, as shown in Fig. 2a. This has been used as filler material and doped with PMMA, as shown in Fig. 2b. When both GNPs doped PMMA were studied under SEM, it was seen that GNPs were dispersed uniformly throughout the area of 30 mm \times 20 mm. The SEM image was taken at a magnification of 600X. After spray coating, the sensor was set for drying at room temperature. Here, GNPs are adhered nicely to the surface of SS304. Figure 2d is the enlarged view of GNPs attached to the PMMA substrate at a magnification of 5000X. These GNPs act like piezo sensors while doing fatigue testing. Raman testing has also been performed to confirm GNPs doped PMMA. Here, Raman, being a smart non-destructive technique (NDT), confirms the presence of graphene and PMMA by the location of their respective falls in the range of wavenumber. As

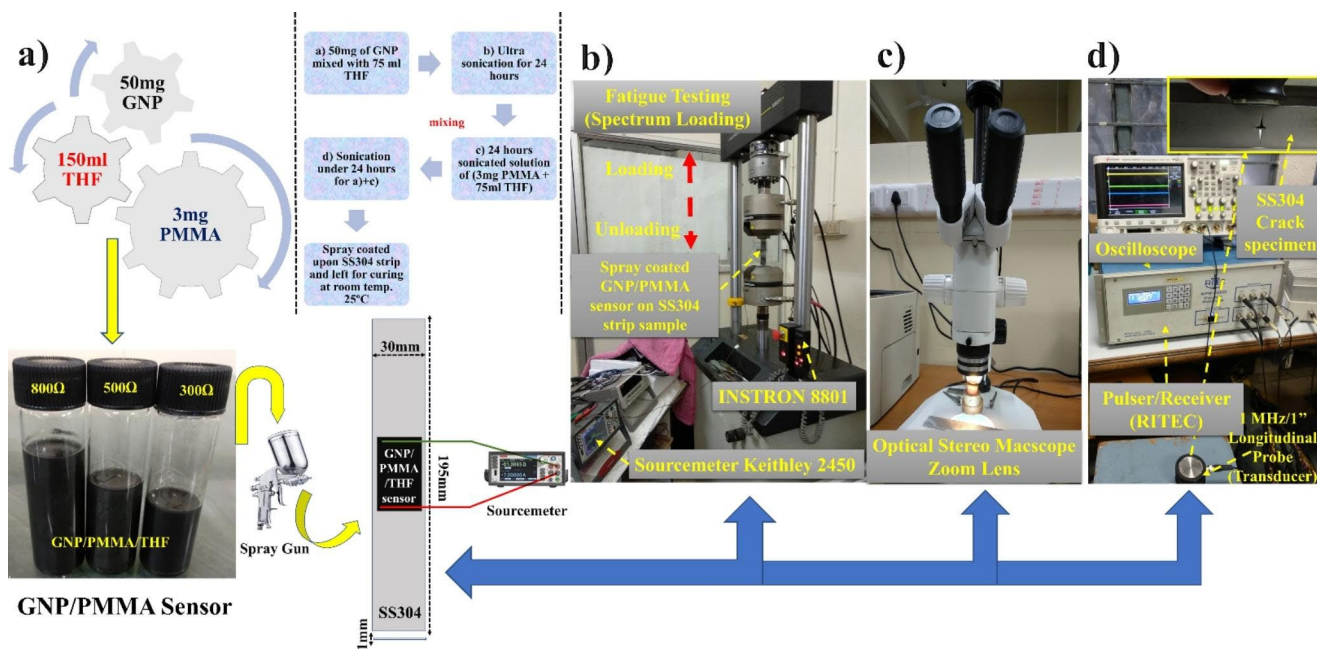


Fig. 1 a Fabrication of GNP smart layer on SS304 strip (area of 30 mm×20 mm size was chosen at the close proximity of SS304 (with defect and without defect region)) b Experimental setup (INSTRON-8801) to do spectrum fatigue testing on the SS304 strip

(with and without damage) c Optical stereo zoom macroscope for measuring crack length after fatigue testing d Ultrasonic testing by ToF method for measuring crack location (RITEC with the oscilloscope and 1 MHz longitudinal transducer)

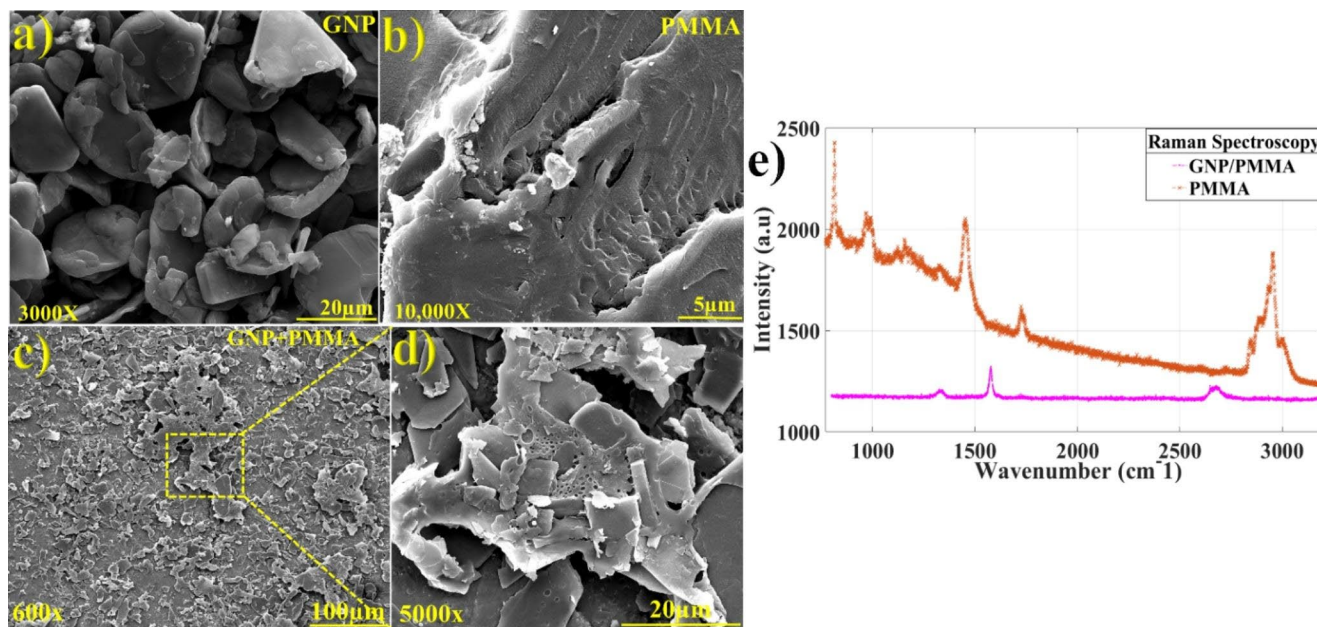


Fig. 2 SEM images of GNPs and PMMA at different resolutions: a GNPs (3000X magnification with 20 μm resolution). b PMMA as the substrate at a magnification of 10000X c and d GNPs doped into

PMMA after dispersion with THF e Raman spectroscopy for the identification of GNPs and GNP doped PMMA

shown in Fig. 2e, the D-peak lies in wavenumber 1367 cm^{-1} . This D-peak is due to a disorder in translational symmetry during mechanical cleavage. This confirms the presence of GNPs in PMMA. Similarly, G-peak due to vibrational motion arising from GNPs stacking lies in the wavenumber

of 1560 cm^{-1} . 2D peak (G^2 -peak) due to 2nd order boundary phonons lie at 2734 cm^{-1} . These are the fingerprints for the confirmation of GNPs in Raman spectroscopy. Also, for PMMA, it can be seen from Fig. 2e, that there is the

presence of CH_2 at 853 cm^{-1} , O-CH_3 at 999 cm^{-1} , C-H and O-CH_3 at 1460 cm^{-1} , and CH_2 at 2957 cm^{-1} .

4 Results and Discussion

4.1 Spectrum Load Monitoring by GNPs/PMMA Sensor

First, SS304 specimens were spray-coated with GNP-doped PMMA sensors. First, the nitrogen/air cylinder was connected to the spray gun inlet, and 6 Psi was maintained by the pressure control knob at room temperature, $25\text{ }^\circ\text{C}$. There is chamber storage in the spray gun as shown in Fig. 1, that leads to the outlet nozzle head. When the inlet trigger is pressed, the chemical is atomized into fine droplets, settling onto the specimen surface. Then they were cured for 24 h at room temperature ($25\text{ }^\circ\text{C}$) for drying. Then the sensors were maintained at initial resistances of $300\ \Omega$, $500\ \Omega$ and $800\ \Omega$ by the scotch tape erosion method. It is a mechanical cleavage technique for maintaining the initial resistance of the GNPs sensor. Then the GNPs/PMMA coated specimens were tested under monotonic load to check sensitivity. The samples were loaded within the elastic limit to a strain of 0.14% at a crosshead displacement rate of 1 mm/min . It was found that concerning (w.r.t) strain increment, the normalized resistance of all specimens increased linearly. The GNPs coated sample with high initial resistance at $800\ \Omega$ has shown better sensitivity to strain. The highest sensitivity, or gauge factor (GF), obtained is 84. As R_0 (intrinsic resistance) decreases gradually, the GF decreases as the slope of the curve fitting decreases, which signifies the sensitivity decline. The sensors with R_0 $300\ \Omega$, $500\ \Omega$ and $800\ \Omega$ have shown GF of 11 ± 0.5 , 37 ± 2 and 84 ± 1 , respectively. These sensors have shown the highest GF compared to an industrial strain gauge (HBM1-LY41-6/350 ($R_0 = 0.35\text{ k}\Omega$; measured GF is ~ 1.6)). In the context of crack monitoring potential, a graphene-based sensor helps to monitor crack propagation in terms of piezoresistivity. Here, monitoring crack propagation is the major concern to be sensed by graphene and ultrasonic transducer. Two different methods have been compared: smart non-destructive testing approach by graphene sensor and ultrasonic sensor. It has been found that graphene sensor is more sophisticated in avoiding material failure in online monitoring than in detecting after failure by an ultrasonic transducer. Here in this article, graphene has helped in detecting crack propagation. This crack monitoring is complicated by an ultrasonic transducer after three times of spectrum loading, as described in the article. In Sect. 4.2 and 4.3, the stress acting upon sensor particles has been experimented with and verified by simulation with XFEM modelling. This stress helps

in developing piezo-resistivity between the sensor and the specimen. Hence, crack propagation leads to a change in resistance behaviour.

Generally, crack growth involves nucleation, growth, and coalescence voids at a crack tip. Here, crack growth occurs due to the release of stored elastic strain energy. This thermodynamic driving force for fracture leads to dissipation of energy that includes plastic dissipation and surface energy [38]. Plastic deformation at the crack tip usually depends primarily on the specimen's applied stress direction, crack length and geometry. Here in the spectrum loading, the crack is present at every stage of frequency where the crack undergoes cyclic loading. Therefore, the specimen plastically deforms at the crack tip. Here in the spectrum loading done upon the SS304 specimen, due to overload, a crack grows out of the plastic zone and leaves behind the original plastic deformation. As shown in Fig. 3c, the graph position with respect to time says about the spectrum cyclic loading, which itself is a position-controlled mode. In the design process of cyclic testing, 9 blocks of spectrum loading were planned in this experiment through the wave matrix software of UTM (INSTRON 8801). These blocks can be visualized in Fig. 7a. So, during tensile loading, the specimen gets stretched apart, and as a result, due to quantum mechanical tunnelling, conductivity takes place between GNPs. With an increment in distance between GNPs particles, the resistance increases; hence, GF also increases. This can be well observed in Fig. 3a. Here the highest GF 84 from the $800\ \Omega$ sensor is picked up for sensitivity analysis in spectrum fatigue loading. As seen in Fig. 3c, the spectrum fatigue cycle was designed for 9 blocks. Each packet of the spectrum fatigue cycle was controlled with different position modes at different amplitudes with a constant frequency of 0.1 Hz . The first block of the spectrum fatigue cycle was for 0.4 mm for 1 cycle. This then changed to 0.2 mm for 1 cycle, then 0.3 mm for 6 cycles, 0.4 mm for 1 cycle, 0.5 mm for 6 cycles, 0.4 mm for 1 cycle, 0.3 mm for 6 cycles, 0.2 mm for 1 cycle and 0.1 mm for 6 cycles. So, during this kind of random loading, the resistance also changes because of pressure-induced behaviour at the interface between the GNPs and the SS304 specimen. This piezoresistive action brings the GNPs particle to get oriented in a random direction during the stretching and compressive action of load. Hence, the GNPs get disoriented, and their resistance behaviour changes, and it takes a long time to come back to their resistance value. As observed from Fig. 3b, in the 1st spectrum loading, in the time interval of $0\text{--}70\text{ sec}$, the amplitude peak reaching baseline shifting is 2.12% for the first 6 cycles. Suddenly, the peak height amplitude shifted to 8.7% and remained constant for the rest of the consecutive cycles for the next 70 sec . After that, the peak from the baseline shifted to 8.93% , and it constantly went up to 108 sec , then

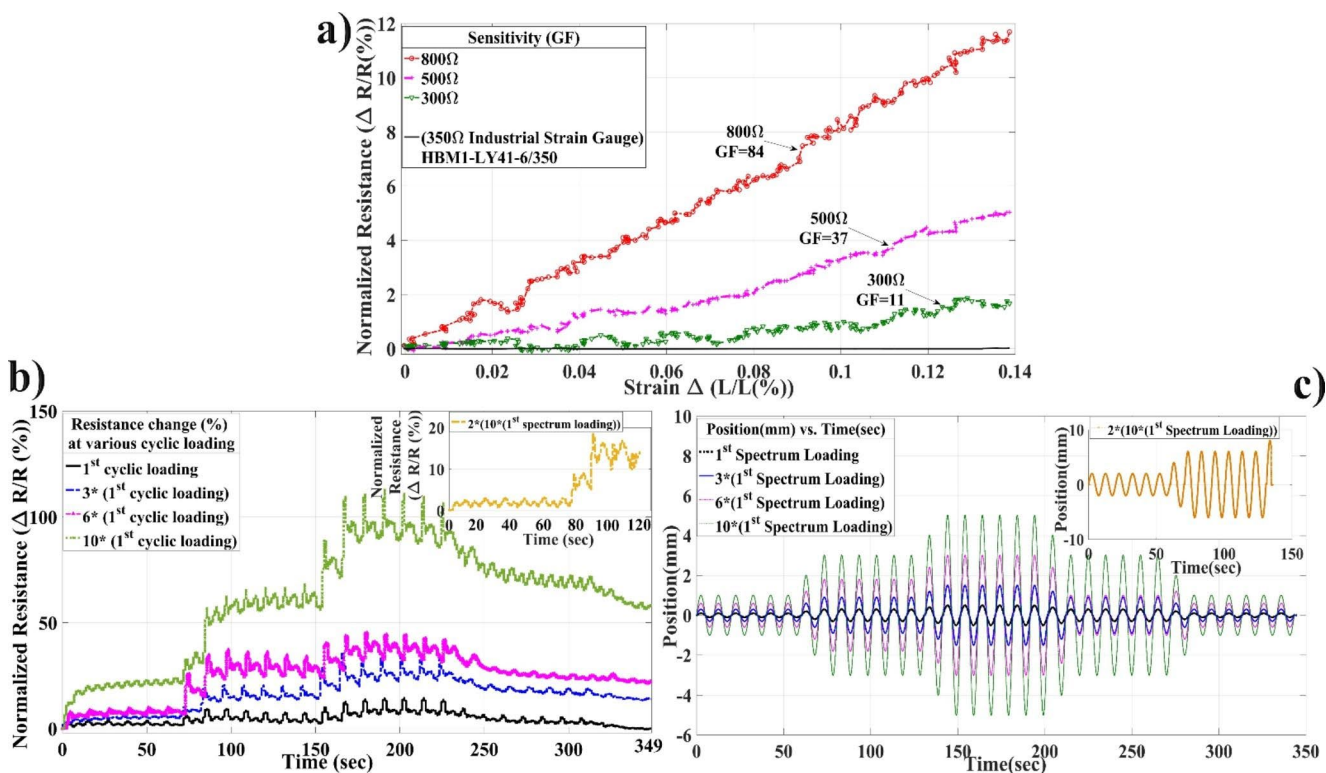


Fig. 3 Sensitivity analysis during monotonic uniaxial loading and piezoresistive action during spectrum loading: **a** Graph showing Sensitivity (Gauge Factor) **b** Normalized resistance (%) w.r.t time (sec)

during spectrum fatigue loading **c** Position (mm) vs. time (sec) during spectrum loading

it declined slowly to 7.38 % at 121 sec and continued up to 144 sec. Then suddenly, with an increment of amplitude, the resistance again increased to 9.213 % at 155 sec for 1 cyclic load and then normalized resistance increased to 12.16 % and then $\Delta R/R(\%)$ (normalized resistance) increased to 13.85 % at 180 sec and remained constant up to 225 s and then declined to 8.9 % at 238 sec, and then after 250 sec, the amplitude decreased, which made GNPs resistance decline as the GNPs particles could not move away from each other like they used to be at higher amplitudes. This causes GNPs particles to stretch and compress with a lower amplitude, lowering sensitivity with low baseline shifting. So, after 250 sec, the $\Delta R/R(\%)$ changed to 6 %. At 261 sec, the $\Delta R/R(\%)$ is changed to 4.66 % at 306 sec. At 342 sec, $\Delta R/R(\%)$ is changed to 0.3 % and reaches to original resistance at 344 sec with 0 % baseline shifting. Similarly, for 3 times*(1st spectrum loading), the peak amplitude from baseline shifting is greater as compared to the previous one for the same time interval of 0–70 sec. The baseline shifted up to 5.8 %. Then, after an increment of further cyclic load, the basement shift is increased to 10 % at 71 sec. Then the baseline is shifted more to 18.68 % at 83 sec and remained constant up to 142 sec. Then, with an increment of higher amplitudes, the peak from baseline shifted more to 28 % at 154 sec. Then slowly, it then increased to 35 % at 165 sec

and stayed up to 211 sec. After 211 sec, the peak amplitude at 223 sec from baseline is shifted to 32.62 %. Then, after 230 sec, the peak level of amplitude from the baseline shifted with a declining slope at peak amplitude to 26 %. Then, in between 250 and 300 sec, the peak amplitude from baseline shifted to 19 % and remained constant. This then declined to 14 % at 343 sec. This baseline shifting at the end of cyclic loading indicates particles are not oriented to a uniform direction like before because of misorientation during piezoresistive action. When the spectrum loading is increased to 6 times of 1st spectrum loading, the baseline of the peak is shifted to 9.43 % from 0 to 63 sec constantly. Then, after 63 sec, the baseline is shifted for higher amplitude cycles to 25.76 %. When again this cycle enters to 3rd block of cyclic loading, the baseline is shifted to 34.89 % at 86 sec and again is increased in consecutive 2nd cycle of this block at 98 sec and remained constant after it for five cycles for 36.19 % from 110 to 120 sec. Then again, it is declined to a baseline peak, shifting to 226 s from 44%, followed by 44.5–41.97 % and then declined to 38.69 % at 232 sec. Then this declined to 34.6 % at 244sec and further declined to 25 % at 325 sec and finally declined to 22 % at 344 sec. Similarly, for 10 times (1st spectrum loading), the baseline shifting is 20.12% and is in between 0 and 66 sec. Then suddenly, the baseline shifting starts moving with a

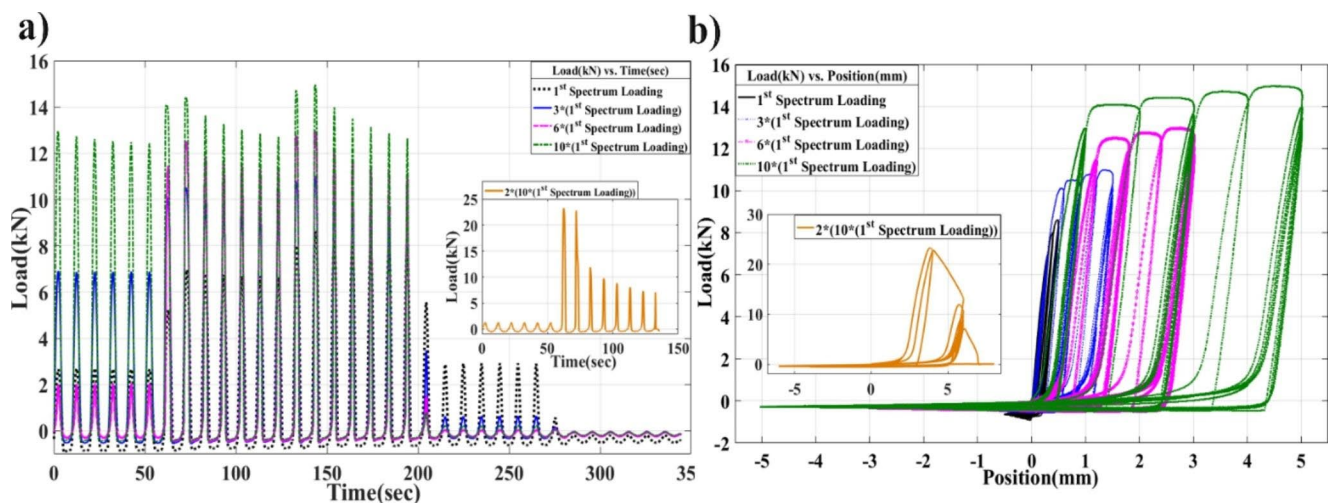


Fig. 4 Spectrum Fatigue loading showing mechanical parameters: **a** Graph showing load (kN) vs. time (sec) **b** Load (kN) vs. position (mm) showing hysteresis loop at different stages of fatigue loading

higher amplitude for further cyclic loading. So, at 72 sec, the baseline shifted to higher peak amplitude of 32.5%, and it is continued for up to 35.9 % at 78 sec. When the cycle entered to 3rd block of spectrum loading, the peak of the baseline shifted to 56.95 % at 85 sec. The maximum peak is reached at 120 sec, with a 66.44 % increase in peak amplitude. When the cycle entered the next block of loading, the peak amplitude rose to 88.76 % at 155 sec. It remained constant for 109.4 % of the time between 180 and 214 sec. Then the peak amplitude of the baseline shifted to 85.78 % from 243 sec to 74.45 % followed by 75.75 % from 250 to 306 sec. After 306 sec, the load amplitude rose to 71.78 % from 312 to 348 sec. When the position-controlled mode was set for $2^*(10^*(1^{\text{st}} \text{ spectrum loading}))$, then the peak with baseline shifted to 1.9% at 4 sec and gradually continued to maintain a constant peak of 3.2 % at 20 sec to 2.937% at 67 sec. Then, with an increment of the next amplitude peak, the load is increased to 8.7 % at 74 sec to 18.49 % at 85 sec. Gradually, when it reached a failure state, the peak resistance declined to 16.28 % and fell to 14.29 % at 113 sec.

4.2 Spectrum Cyclic Study with Hysteresis Loop and Optical Macscope Stereo Zoom Lens Study

Stress-strain curve behaviour obtained from a monotonic test can be quite different from that obtained under cyclic loading. In the case of fatigue testing according to the Bauschinger effect, yield strength is lost because of repetition in tension and compression. Whenever a load is applied in the opposite direction, there is a chance of inelastic deformation which cannot be recovered upon unloading. The strain that is developed by fatigue comes from both elastic and plastic strain. So, stress-strain behaviour in metals can be changed by a single reversal of one inelastic strain.

As shown from Fig. 4a and b, it tells us about the mechanical deformation happening in the SS304 strip in terms of hysteresis loop from load w.r.t position graph and also from load w.r.t time data. As seen from Fig. 4a, load vs. time data has been plotted, revealing how the load varies under the position-controlled mode spectrum fatigue test. The load randomly varies with respect to time due to plastic and elastic strain during spectrum fatigue.

From the load vs. time graph, it is clear that in the 1st spectrum loading, the load rose to 2.55kN and remained constant till 50 sec. Then the load is increased to 5.05 kN at 63 sec, increasing to 6.82 kN and remaining constant till 72 sec. After 83 sec, the load decreased to 6.6221 kN and remained constant up to 123 sec. Then the load is increased to 7.74kN at 133 sec. This increment is because of the tensile nature of spectrum fatigue. Again, after 143 sec, the load is suddenly increased to 8.61 kN. This is the maximum load that was achieved, which then declined to 8.10 kN at 153 sec. This load is then again declined to 7.97 kN at 184 sec. Then there is a drastic drop in the load to 5.46 kN at 204 sec and further declines to 2.63 kN at 214 sec. It remained constant for 2.63 kN up to 255 sec. The load then fell completely to 0.135 kN at 276 sec. From 286 sec to 343 sec, the load was completely compressed to -0.21 kN. Consequently, if load vs. position data is analyzed from Fig. 4b, then it will be seen that because of the reversal plastic strain, the load-position behaviour changes as reverse loading causes the material to bend a lot, which couldn't be recovered back and hence load in the reverse direction couldn't reach the same limit as compared to tensile action during fatigue testing. The load in the upper limit reached 3.40 kN during the first cycle of the 1st spectrum loading between 0 and 9 sec, despite the fact that the position was only ± 0.104 mm due to position-controlled mode. And in

the reverse direction load reached to -1.37 kN. This not only changes the stress-strain behaviour but also helps in reducing the stiffness of the SS304 because of bending. After 110 sec, the hysteresis loop also changed a lot as the load rose. Although the load rose strongly to 9.97 kN in tensile action and reverse loading, the load declined to -1.31 kN in the position range of ± 0.302 mm. Then, at 150–300 sec, the load-position graph changed slightly in 3 stages. First, the load reached the upper limit of 15 kN at 0.49 mm and reversed to a load of -1.29 kN at -0.49 mm. Then, in the position range of ± 0.4 mm, the load value increased to 12 kN in tensile loading, and the compressive nature load fell to -1.2 kN. Then the load fell to 9.24 kN in tensile behaviour and -1.25 kN in compressive action in the position interval of ± 0.3 mm. Then in the 343–350 sec interval, the load reached -0.16889 kN at a position of 0.008451 mm, which on complete decrement fell to -1.31 kN at the origin at the end of the cycle. Similarly, for the 3* (1st spectrum loading), the load of 6.89 kN started acting from 0 to 50 sec, suddenly increasing to a load of 10.1 kN at 62 sec. Then the load increased to 10.46 kN at 72 sec, falling to 9.4648 kN at 123 sec. Then the load suddenly increased to 10.68 kN at 133 sec. Then, with an increment of tensile stress, the load is increased to 10.77 kN at 144 sec. The load began to fall to 10.19 kN at 153 sec and then to 9.48 kN at 194 sec due to compressive stress. In the load vs. position graph, between 0 and 10 sec, the load is increased to an upper limit of 2 kN with an extension of 0.3 mm and declined with the same extension with the load reaching -0.55 kN in the reverse direction. The extension is then increased to 0.9 mm with a maximum upper limit load of 15.48 kN and a reverse direction load of -0.9 kN between 110 and 120 sec. Within the extension range of ± 1.5 mm, the load increased to 20.80 kN in the tensile direction and decreased to -0.83 kN in the compressive direction between time intervals of 150–300 sec. Slowly, the load declined to 20.16 kN and -0.85 kN within an extensive range of ± 1.4 mm in tensile and compressive action, respectively. Then again, it decreases to a tensile load of 14.46 kN and a compressive load of -0.84 kN within an extensive range of ± 1.2 mm. And this load decrement continued to 7.16 kN and -0.84 kN within an extension of ± 0.89 mm. At the 343–350 s interval, the load is decreased again to -0.41 kN and -0.48 kN in compressive nature at the last cyclic load of this spectrum loading. The spectrum loading has been increased to 6* (first spectrum loading). At the very beginning of 0–52 sec, the load is increased to 2 kN and then, with a sudden increment of tensile action load, is increased to 11.13 kN at 63 sec. With more tensile action, due to extension, the load is increased to 12.32 kN at 73 sec and due to the compressive nature in the reversal bending action, the load further declined to 11.21 kN at 123 sec.

Then the load suddenly rose to 12.95 kN because of tensile action at 143 sec and declined to 11 kN at 194 sec.

Then again, after the reversal in load direction w.r.t position, load declined to -0.21 kN between 218 and 343 sec. This can be well described in Fig. 4b, where it can be seen that load in between 0 and 9 sec reached a maximum limit of 12.63 kN and reached -0.8 kN after reversal within an extension of ± 0.6 mm. After 110–120 sec, the load increased to a maximum of 21 kN, and, in the reverse direction, it went down to -0.77 kN. The position is extended again here to ± 1.8 mm. Due to the repetition of tensile and compressive behaviour, the load increased to 23 kN in the upper limit and -0.651 kN in the lower limit due to an extension of ± 3.007 mm in the time interval of 150–300 s. The load then declined to 21.41 kN at the upper limit and -0.65 kN in the reverse direction at the lower limit of extension to ± 3.001 mm due to the compressive action of the load and the bending phenomenon of strip SS304. Again, because of one more reversal cyclic load, extension is reduced to ± 2.4 mm with the decrement of load to 11.5 kN in tensile and -0.66 kN in compressive action. Then at 343–350 sec, at the end of the last cycle, the load fell down to -0.28 kN and -0.32 kN within a position interval of 0.02 mm and -0.09 mm, respectively, due to compressive action. Now when the position mode is increased to 10* (1st spectrum loading), the load is increased to 12.869 kN from the very initial stage but starts declining at 52 sec to 12.36 kN. But when the position amplitude is increased gradually, the load is also increased from 13.51 kN at 62 sec to 14.29 kN at 73 sec. Then, the load and position vary with the material's stiffness reduction and progressive decrement in the diameter along the major and minor axes due to repetitive tension and compression around the hole. Then the load is decreased to 12.59 kN at 123 sec. Then, with an increment of tensile action, the load is increased to 14.44 kN at 133 sec, which is further increased to 14.96 kN at 143 sec, and suddenly, because of compressive action, the load is decreased to 12.56 kN at 194 sec. Then the load suddenly fell drastically to 0.66 kN at 204 sec. When compressed fully, the load declines rapidly to 0.02 kN from 216 to 265 sec; hence, the last load declines further to -0.022 kN from 281 to 343 sec. If a load vs. position graph is examined, the first cycle load is reached at 0.31 kN to a maximum extension of 1 mm between 0 and 9 sec, and the reverse direction load almost reaches -0.31 kN to the same extension of -1 mm. At 110–120 sec, the load increased to 12.5 kN with an extension of 3 mm and in the reverse direction to -0.57 kN after compression reaching the same extension. Between 150 and 300 sec, the load increases to 22.95 kN in tensile action and decreases to -0.65 kN in reverse action within a ± 3 mm extension. Then with progressive action of compression, the load is reduced to 21.6 kN to the upper limit and declined to -0.65 kN within

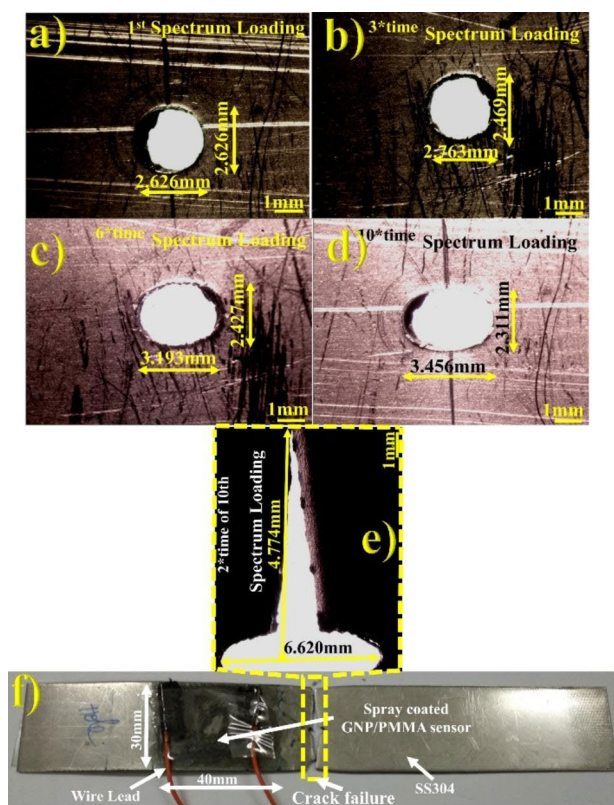
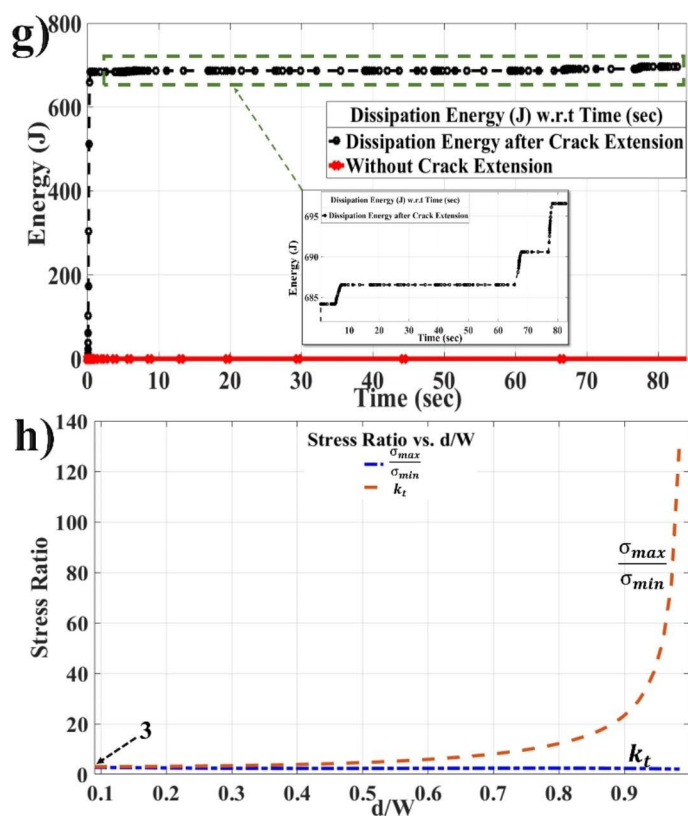


Fig. 5 Crack growth due to spectrum Fatigue: **a-f** Graph showing Optical Microscopy study for crack extension **g** Graph showing Dissipation of Energy(J) vs. Time (sec) with and without crack extension **h**

an extensive range of ± 3 mm. Then, on further loading and unloading at the next step, the load declined from 11.86 kN at the upper limit to -0.66 kN at the lower limit within the extension range of ± 2.4 mm. Then, at a time interval range of 344–350 sec, the load is further declined to -0.25 kN and again declined in the reverse direction to -0.26 kN within an extensive range of ± 0.006 mm. This ends the cyclic loading after 350 sec. When the load is increased to twice the value of (10*(1st spectrum loading)), it fails after 93 sec and fully detached from the crack area fully after 110 sec. In the very beginning, 10 sec, the load is increased because of the maximum position achieved by controlled mode. Here, the load reached 23.03 kN at the upper limit and declined to -0.12 kN at an extensive range of ± 2 mm. The load on compressive action in the reverse direction was then reduced to 22.01 kN in the upper limit and -0.16 kN in the lower limit within the same extension time interval of 40–60 sec. because of crack propagation slowly near the locality of the stress field, the stiffness of SS304 is reduced slowly, making no more load to resist during spectrum fatigue loading. At 70–90 sec, the load is increased to 15.01 kN in the upper limit, reaching the extension of 3.85 mm, and 0.07 kN in the lower limit, with an extension reaching -3.92 mm. Then, with progressive action of compressive and tensile loading, the load is further



graph showing stress ratio varying with d/W (diameter of hole upon the width of the specimen) (Test piece with spray coated GNPs/PMMA sensor situated at 13 mm from hole location)

reduced to 6.76 kN at the upper limit and declined down to -0.09 kN at the maximum extension of ± 6 mm. At the failure peak of time interval 90–93 sec, the load is increased to a maximum of 4.63 kN, and extension is shifted more to 5.73 mm in tensile loading from the initial limit of 0.43 kN at the origin. This then failed with a fracture at the opening mode of extension completely. From the load vs. time graph, as shown in Fig. 4a, the load was increased to 22.47 kN at 62 sec and failed after crack propagation at 110 sec.

As seen from Fig. 5a and f, it is explained that a stereo microscope zoom lens has measured the extension of crack growth after each spectrum loading at 6.2X magnification. In Fig. 5a, after the first spectrum loading, the dimension is changed from the initial 2 mm hole diameter to 2.626 mm. Gradually, after each block of testing, the extension of the crack along the major and minor axis of the elliptic hole was measured under the stereo microscope, and the dimensions of crack growth were applied for plotting the stress intensity factor (SIF) as shown in Fig. 5 g. After plotting stress ratio vs. d/w , it was found that the $\frac{\sigma_{max}}{\sigma_{\infty}}$ grows exponentially with the increment of the d/w ratio. And SIF slopes declined down towards the x-axis. As seen from Fig. 5 g, the energy released at the end of the cycle (2*10*(1st spectrum loading)) at each time interval has been analyzed by XFEM

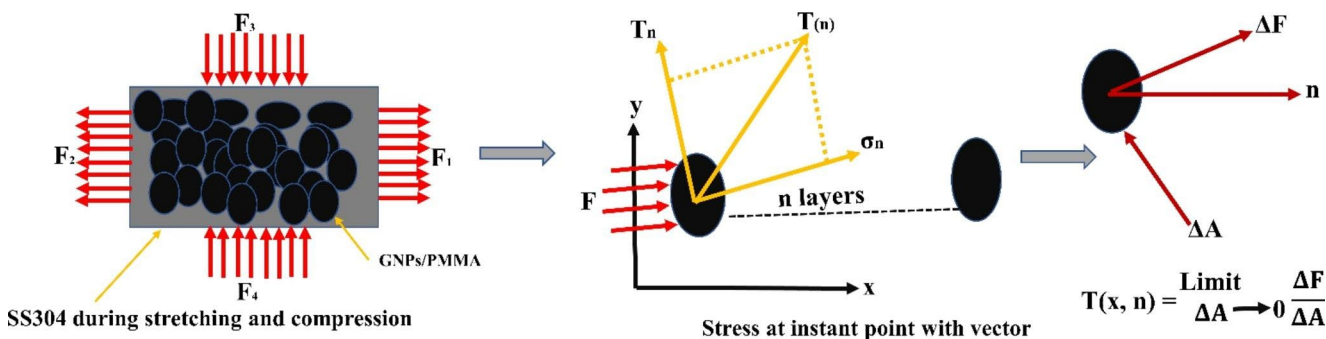


Fig. 6 Schematic of stress arising from SS304 acting upon GNPs doped PMMA

simulation as seen from Fig. 9b. From the energy (J) vs. time (sec) graph, between 0 and 5 s, the energy released was 684.2 J at the beginning of the crack of 2.311 mm along the major axis. During crack propagation at higher cyclic amplitudes, the strain energy was released to 686.5 J at 8th sec and remained constant up to 65th sec; with a maximum growth of the opening mode, the energy was released to 690 J at the 67th sec and remained stable up to 76th sec, and with complete failure, the energy released to 696.5 J at 78th sec. Before crack propagation, the energy released was parallel along the x-axis without any magnitude. Therefore, the maximum energy released was 696.5 J during failure. The force acting on the SS304 specimen at finite width and due to reduction in cross-section because of nominal stress is given by Eqs. 1 and 2 below [39–41].

$$\text{Force} = \sigma_{\infty} w = \sigma_{nom} (w-d) \quad (1)$$

$$K_t = 3 - 3.14 \left(\frac{d}{w}\right) + 3.667 \left(\frac{d}{w}\right)^2 - 1.527 \left(\frac{d}{w}\right)^3 \quad (2)$$

Here, σ_{nom} , is the nominal stress that happens due to the reduction in cross-section near the hole. This can be visualized in Figs. 8a and 9b. Similarly, σ_{∞} , is the remote stress due to uniaxial tension. And ‘w’ is the width of the specimen, and during uniaxial loading, the force developed due to its tensile nature is related to stress as given by force Eq. 1 above. This is expressed with maximum stress, σ_{max} and stress intensity factor (K_t) from Eq. 2 as shown below.

$$\frac{\sigma_{max}}{\sigma_{\infty}} = \frac{\sigma_{max}}{\sigma_{nom}} \times \frac{\sigma_{nom}}{\sigma_{\infty}} = K_t \times \frac{w}{w-d} \quad (3)$$

Here from Eq. 3 and graph of Fig. 5 h, it is observed that $\frac{\sigma_{max}}{\sigma_{\infty}}$ ratio never decreases but $1/K_t$ value continuously decreases with increasing d/w. This says increasing the hole diameter or decreasing the specimen width ‘w’ always increases maximum stress at the hole. This is clearly explained in the XFEM 2-D Modelling Fig. 9.

4.3 XFEM 2D Modelling of Crack and ToF Study by Ultrasonic Test

Whenever stresses act on the specimen, then, because of relative action between the GNPs/PMMA coated sensor and the surface of SS304, stress at a point comes into play. This is because the strain acting at the interface brings stress into

the act. The stresses arising from the hole circumference area act upon the substrate PMMA holding GNPs. Now, these stress vectors act at a given point on the GNPs surface that depends on the orientation of the surface. Here in the FEM model, we have assumed stresses acting in two directions; one is along the forces acting on the specimen SS304, and the other is perpendicular to the plane of force acting on the specimen.

As shown in Fig. 6, fatigue spectrum loading stresses act on SS304 because of its repeated cyclic tensile and compressive nature. So, from the Fig. 6, stresses act in the x-y direction, which makes GNPs strain along with the PMMA substrate that brings relative stress on it and is oriented along with the stress with traction ($T(x, n)$) acting on the GNPs. Now, to know the stress acting on the sensor surface, the FEM model has been studied, taking stress values around the hole’s proximity to the sensor at a distance of 1 mm. So, the 2D static and dynamic XFEM [39–41] models have been simulated by Abaqus 6.12 version CAE software.

Both models have been designed, as shown in Fig. 7a. From Fig. 7c, at locations of, 1,2,3, and 4, stress acting due to spectrum fatigue has been calculated and analyzed as shown in Figs. 8 and 9. The XFEM 2D model has been simulated for crack propagation studies, as shown in Fig. 7b, whose image was taken and measured under optical microscopy. As seen from Fig. 7 b and Fig. 5 d e and f, the crack has been extended to an extra length of 6.092 mm in the major axis (x-direction) and 4.309 mm in the minor axis (y-direction). This crack propagation along the x-axis, as observed from the stress vs. time graph, means that the stress value is more in the y-direction, and because of the release of energy along the x-direction, the stress value is reduced.

As shown in Fig. 8b, in the 1st spectrum loading, because of its tensile nature, maximum stress is 1745 N/m² at 1 sec, and between 0 and 50 sec, the stress started declining to 601.8 N/m² at 44 sec.

And somewhere between 60 and 100 sec, the slope again started declining because of compressive stress. Stresses were found to be -642.5 N/m² at 66 sec and -518.9 N/m² at 100 sec. Then, because of its tensile nature, the stress

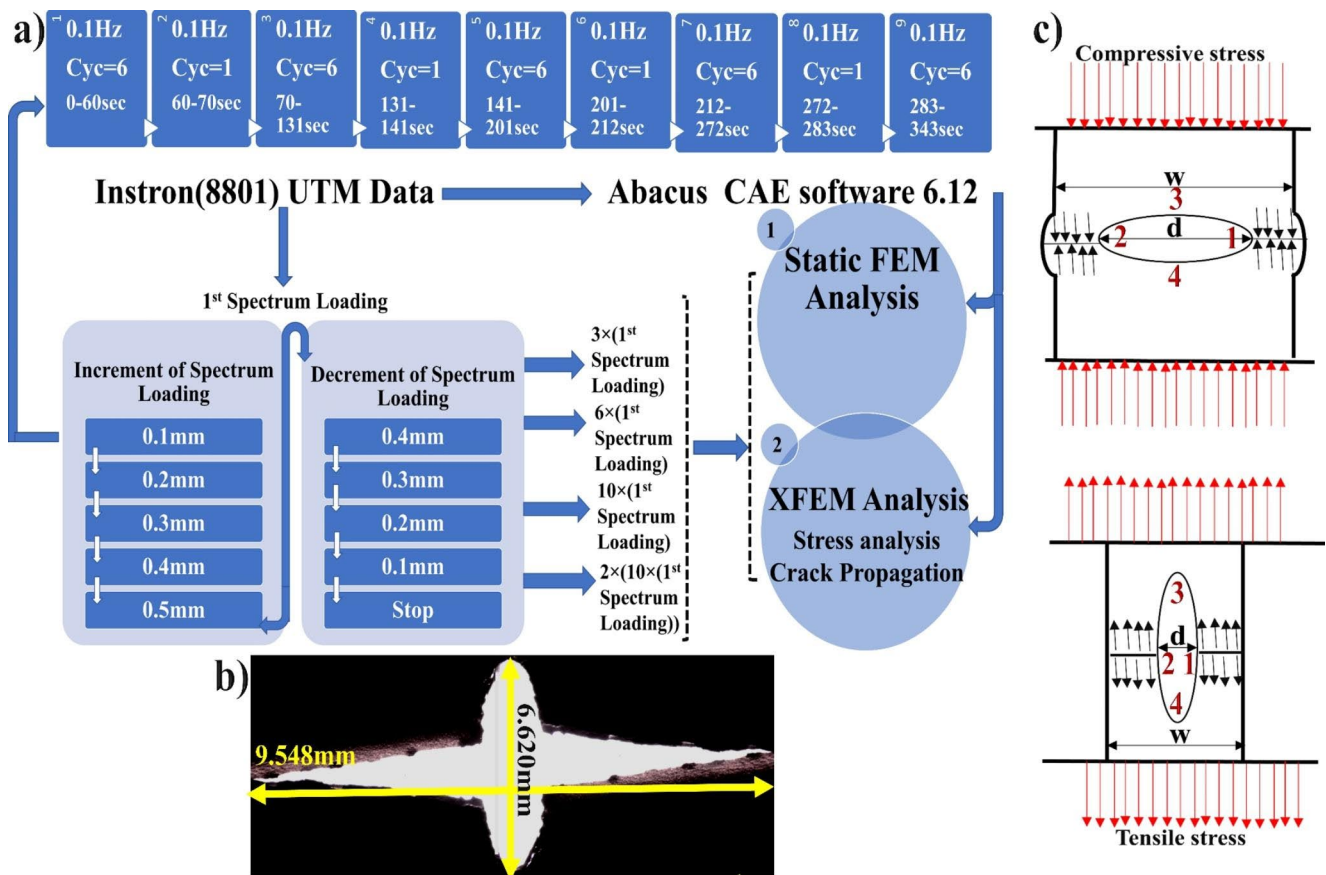


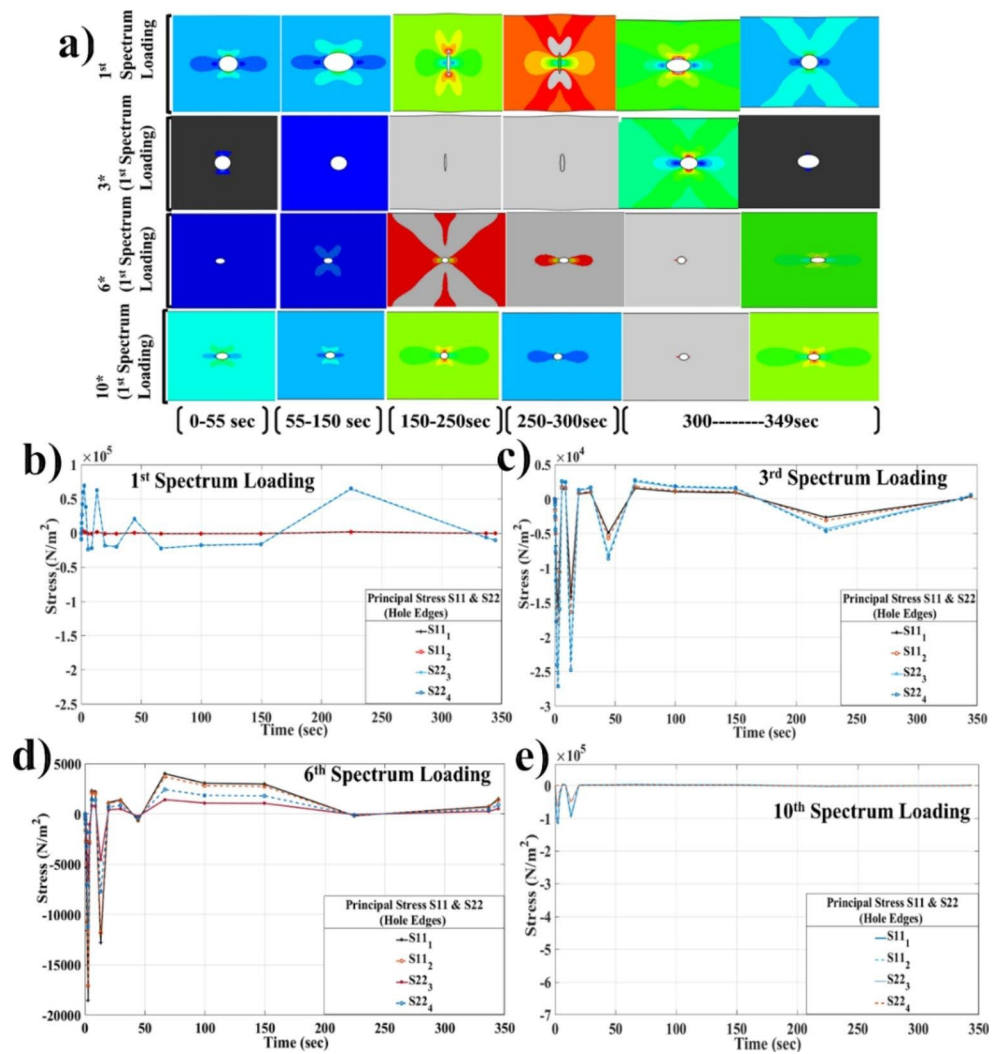
Fig. 7 Spectrum loop blocks diagram interfaced with Abaqus 6.12 software: **a** Graph showing loading parameter for each stage of spectrum cycle and stress-strain data used for simulation in Abaqus software **b**

Optical spectroscopy image at final failure **c** Schematic for repeated cyclic load changing the geometry shape of the hole to an ellipse in the longitudinal and transverse direction

increased to 1901 N/m² at 224 sec and declined slowly to -305 N/m² at 344 sec. This was the same for position 2. Similarly, the stresses in positions 3 and 4 overlap nearly identical. Maximum stresses, in this case, are 6930 N/m² at 2 sec, 63,060 N/m² at 13 sec, and 20,690 N/m² at 44 sec. Then in between 66 and 150 sec, stresses are compressive, where stresses are -16,150 N/m² at 150 sec. And in between 200 and 300 s, maximum stress was 65,340 N/m² and suddenly declined to -6421 N/m² at 336 sec and -10,500 N/m² at 344 sec. Similarly, for 3rd spectrum loading, in between 0 and 50 sec, maximum stress is -15,480 N/m² at 2 sec, and after 50 sec, stress is increased to 1817 N/m² and, because of repetitive tensile and compressive stress, stress fell to 1083 N/m² at 150 sec. Then it completely declined to -3080 N/m² at 224 sec, and stress rose to 417 N/m² at 344 sec. Similarly, at position 2, maximum compressive stress was -17,950 N/m² at 2 sec. Stress is gradually increased to 1630 N/m² at 8 sec with tensile nature. The maximum stress is increased to 1817 N/m² at 66.5 sec and gradually decreased to 1083 N/m² at 149 sec between 60 and 150 sec. because of compressive stress at 224 secs, stress declined and increased again at 344 sec to 417 N/m².

For stresses in the y-direction, the compressive stress reached a maximum in between 0 and 50 sec to -25,320 N/m² at 2 sec, and the tensile stress increased to -8031 N/m² at 44 sec. Then suddenly, the tensile stress reached a peak of 2561 N/m² at 150 sec, the compressive stress decreased to -4342 N/m² at 224 sec, and the stress increased to 588 N/m² at 344 sec. Similarly, between 0 and 50 sec, stress is reduced to -27,140 N/m² at the third sec and increased to -8611 N/m² at the 44th sec. At 66th sec, maximum tensile stress was 2747 N/m² and declined slowly to 1083 N/m² at 149 sec. And at the 224th sec, compressive stress is reduced to -3080 N/m² and is increased to 417 N/m² at the 344th sec. Similarly, in Fig. 8d, in between 0 and 50 secs, maximum compressive stress is -18,520 N/m² at 2 sec, and in tensile nature, maximum stress is 2319 N/m² at 6th sec, and again, because of compressive nature, stress declined to -12,780 N/m² at 13 sec. Then, tensile stress is suddenly increased to 1128 N/m² at the 19th sec. Then, at the 30th second, it is increased to 1402 N/m². Then the stress declines to -669 N/m² at the 44th sec. Then, in between 66 and 180 sec, the tensile nature of the spectrum declined to -184 N/m² at 224th sec. The stress is then increased to

Fig. 8 Principal Stress data near hole circumference zone during shape changing at every stage of spectrum loading obtained from XFEM simulation: **a** Graph showing shape variations from circular hole to elliptic hole at various stages of spectrum loading with respect to time **b-e** Graph of principal stresses w.r.t time



1489 N/m² at 344th sec between 230 and 350 sec. Similarly, position 2 follows, with maximum tensile stress between 66 and 150 sec and maximum stress ranging from 3689 N/m² to 2736 N/m² at the 150th sec. At position 3, the maximum stress was 1417 N/m² at the 66th second and 1051 N/m² at the 150th second before gradually decreasing to -65 N/m² at the 224th second and reaching 528 N/m² at the 344th second. Similarly, for position 4, stresses decreased to -11,220 N/m² after 2 s, increased to 1405 N/m² after 6 s, and decreased to -405 N/m² after 44 sec. Then increased to 2419 N/m² at 66th sec and again started declining from 66 to 224 sec, at 2419 N/m² to 1794 N/m² at 149 sec to -11.5 to 1794 N/m² at 224 sec. And finally, at the 344th sec, stress is increased to 662 to 1794 N/m². When the load is increased to ten times the first spectrum loading, stresses are compressive between 0 and 50 sec and decline to -109,400 N/m² at the next 2 sec. At 13 sec, stresses increase due to tensile behaviour to -90,280 N/m². Similarly, stresses at positions 3 and 4 are -61,390 N/m² and -5297 N/m², respectively, at the 1st and 13th sec. After that, at 100 sec, stress increased

to 1360 N/m² and started declining, which fell to -994 N/m² at 224 sec because of the compressive nature. At 344 sec, stress is increased to 662 N/m². Similarly, as seen from Fig. 9a and c, FEM simulation analyses the stress field around the hole's circumference to see the stress behaviour in the x-y direction. Here in this, the maximum stress is at the 1st sec, that is, -155,100 N/m², which again, after reaching 13th sec, stress is increased to 2133 N/m², which then increased to 2133 N/m² at the 100th sec and 2210 N/m² at the 150th sec. This then declined slowly to -1648 N/m² at 224 sec and increased to 922 N/m² at 344 sec. Similarly, at position 2, maximum stress fell to -180,600 N/m² at 1st sec and then suddenly, due to tensile behaviour, stress increased to a maximum value of 5013 N/m² at 44 sec. Then it declined slowly due to its compressive nature to 4105 N/m² at 66th sec and 2573 N/m² at 150th sec. Then, because of compressive stress, the stress came down to -1919 N/m² at 224 sec, which increased to 1073 N/m² at 344 sec. At positions 3 and 4, the stresses are almost overlapped. Here at 1 sec, stress is -46,980 N/m², which is increased to 1073 N/m² at 344 sec.

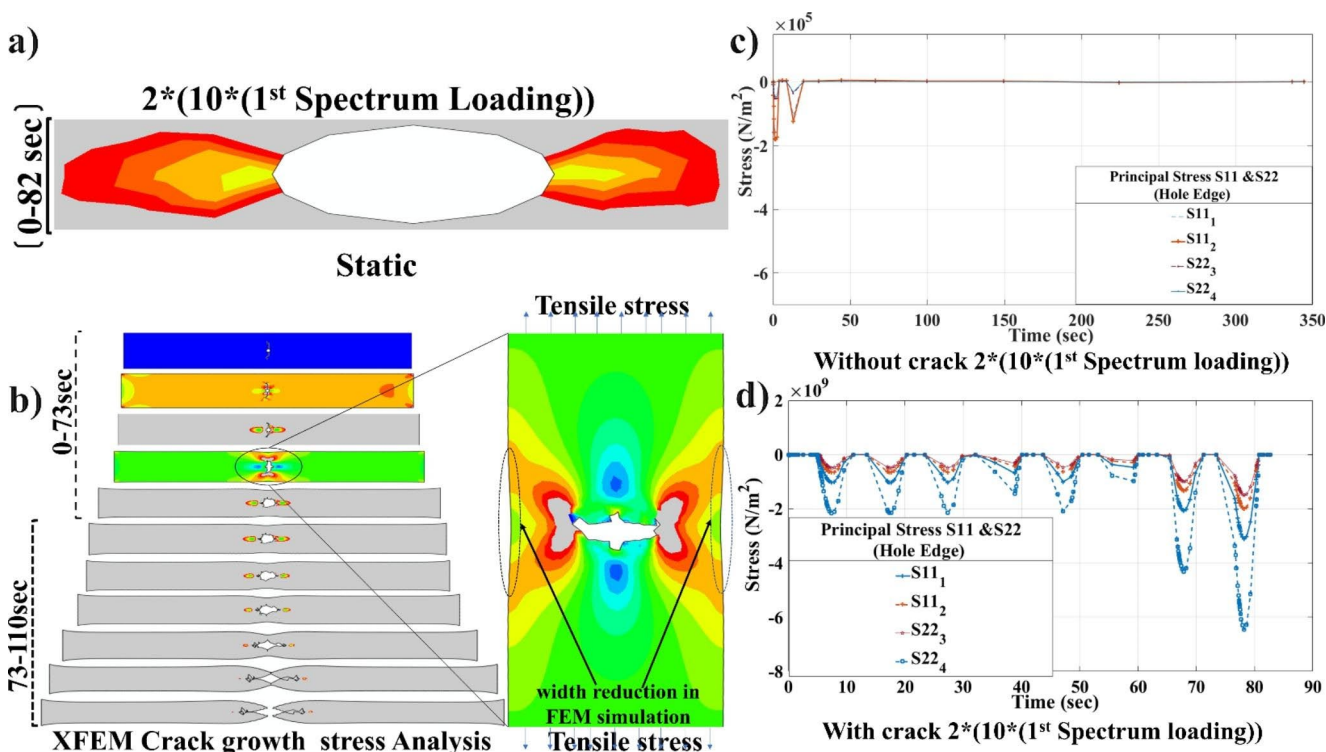


Fig. 9 FEM simulation by Abaqus 6.12 software for spectrum loading at static and dynamic conditions: **a** Graph showing static stress field without crack development around edges of hole during 0-82 s at final stage of spectrum fatigue (2*(10*(1st spectrum loading)) **b**

XFEM simulation using abaqus software for crack propagation showing stress field around crack tip point in 0-110 s **c-d** Principal stresses around stress field near crack zone

At positions 3 and 4, the stresses are almost overlapped. Here, stresses are $-46,980 \text{ N/m}^2$ at 1 sec and $-32,368 \text{ N/m}^2$ at 13th sec, and thus stresses gradually increase to 652.9 N/m^2 at 20th sec, 1340 N/m^2 at 44.3 sec, and slowly decline to 646 N/m^2 at the 100th sec, increased to 669 N/m^2 at the 150th sec, and slowly declined to 279 N/m^2 at 344 sec. In the XFEM simulation, stress data was analyzed as seen from Fig. 9b-d, where it is observed with crack propagation that not only the energy after release is acting on GNPs but also stresses are acting at different points on GNPs, which is the main cause for GNPs to disorient from their original position. Hence, this affected the normalized resistance to shifting more from the baseline position, and it did not come back to its original position after the end of the cyclic test. In the dynamic XFEM crack analysis, the stresses are reduced due to the release of energy at positions 1 and 2 because of crack propagation. Hence, stresses are reduced in the x-direction. But in the y-direction, the stress values are higher than the x-direction, as observed in Fig. 9d. In the y-direction, the crack propagation is not there as the force applied is along the y-direction and crack propagation is always perpendicular to the force direction. In this case, stress is decreasing in the x-y direction. Maximum compressive stress is $1034 \times 10^9 \text{ N/m}^2$ in the x-direction at position 1, and it decreases to $-2.08 \times 10^9 \text{ N/m}^2$ at the 68th sec. And

after full failure, when the specimen is fully broken, the tensile stress is reduced, pulling down the compressive stress with a magnitude of $-3.117 \times 10^9 \text{ N/m}^2$. Similarly, for position 2, maximum stress is $-6.608 \times 10^8 \text{ N/m}^2$ from 7th sec to $-6.59 \times 10^8 \text{ N/m}^2$ at 27th sec. In between time intervals of 40-60 sec, the crack propagation is not uniform, and finally, after 68th sec, stress declined to $-1.336 \times 10^9 \text{ N/m}^2$ and further to $-2.01 \times 10^9 \text{ N/m}^2$ at 78th sec. At position 3, there is less opening mode along the major axis, propagating fewer cracks with less energy release. So, the stress acting here is slightly higher than in positions 1 and 2. In between 8th sec and 28th sec, stresses increased to $-4.835 \times 10^8 \text{ N/m}^2$, whereas stresses fell to $-9.975 \times 10^8 \text{ N/m}^2$ at 68 sec and to $-1.505 \times 10^9 \text{ N/m}^2$ at 78th sec during failure. At position 4, stress acting is very low, that is, $-2.151 \times 10^9 \text{ N/m}^2$ and remained constant up to the 27th sec. And due to the maximum opening mode because of repetitive tensile and compressive stress, the stress is reduced to $-4.316 \times 10^9 \text{ N/m}^2$ at the 67th sec, and during failure, stress is declined to $-6.463 \times 10^9 \text{ N/m}^2$ at the 78th sec. To understand the physics of wave interaction defects at various loadings, we have modelled ultrasonic experiments using FEM software (Abaqus 6.12). The simulation results obtained from wave propagation upon SS304 under various spectrum loadings are shown in Fig. 10.

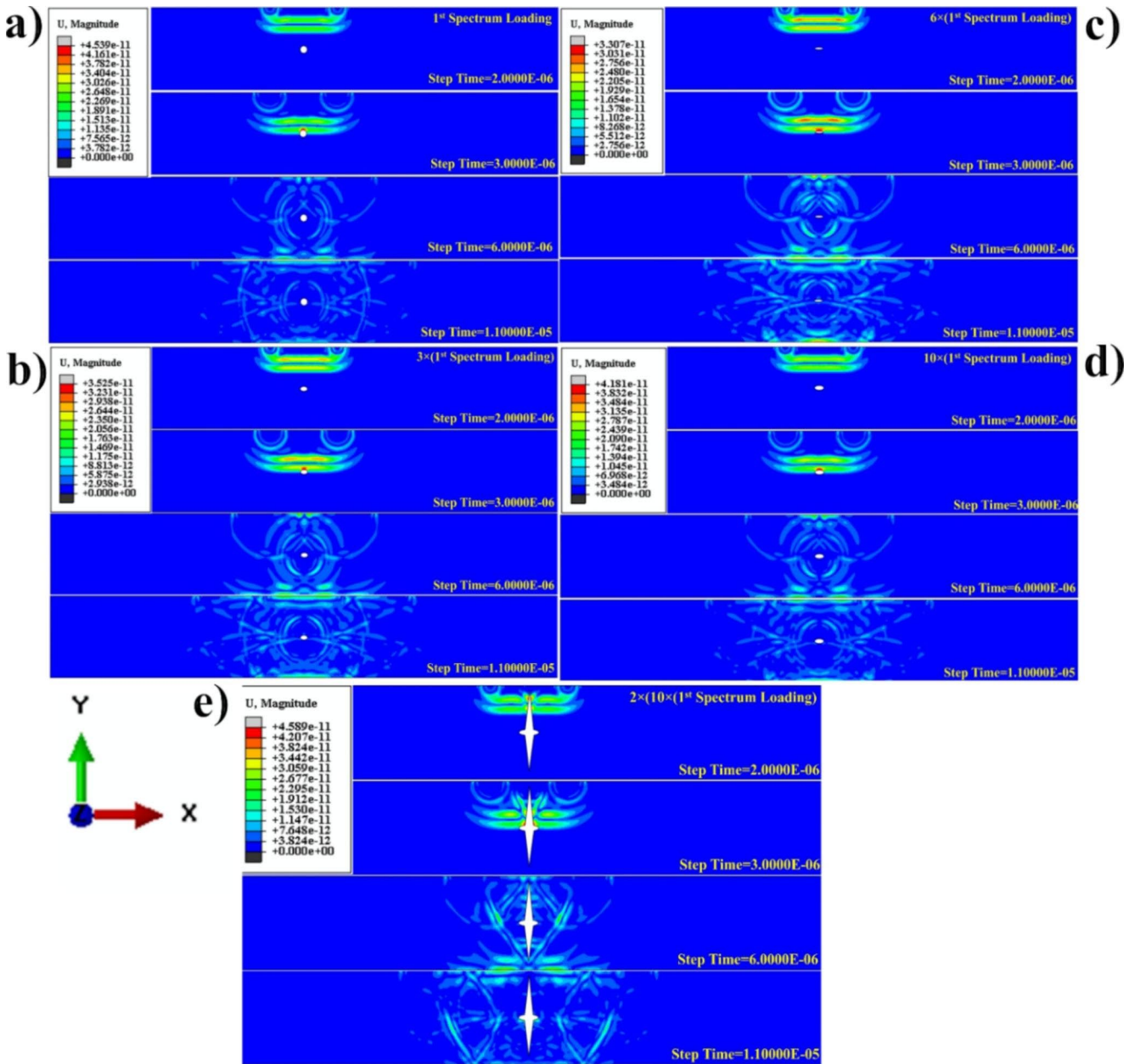


Fig. 10 Simulation of wave propagation around crack from source node by Abaqus 6.12 software: **a-e** graph showing wave interaction for 1st spectrum loading, 3* (1st spectrum loading), 6* (1st spectrum loading), 10*(1st spectrum loading) and 2times (10*(1st spectrum loading))

As seen in Fig. 10a, the wave propagation takes place from the effective radius of the longitudinal transducer (Panametrics-NDT/V102/1MHZ/1”) to the circumferential edge of the hole. The ultrasonic waves are first excited by the transducer, which interacts with the hole after travelling a time difference of 5.8 μ sec. At the step time of 3 μ sec, the incident waves interacted with the hole’s circumference, where the hole dimension changed to 2.626 mm after the 1st spectrum loading from the initial dimension of 2 mm. After this interaction, the waves were scattered from the boundary of the hole, which interfered with incoming

waves even after reflection from the other end of the specimen’s width. This can be seen from the step time of 6 μ sec. At 11 μ sec, the interaction of the back wall reflected waves with the incoming waves from the transducer and with scattered waves from the outer edge of the hole increased with interference. Hence, detection can be visualized from TOF Fig. 11b.

Similarly, for 3rd spectrum loading, the interaction of incident waves from the transducer with the edge of the hole is more destructive than the 1st spectrum as the hole becomes elliptic. So, the ellipse’s edge makes the wave

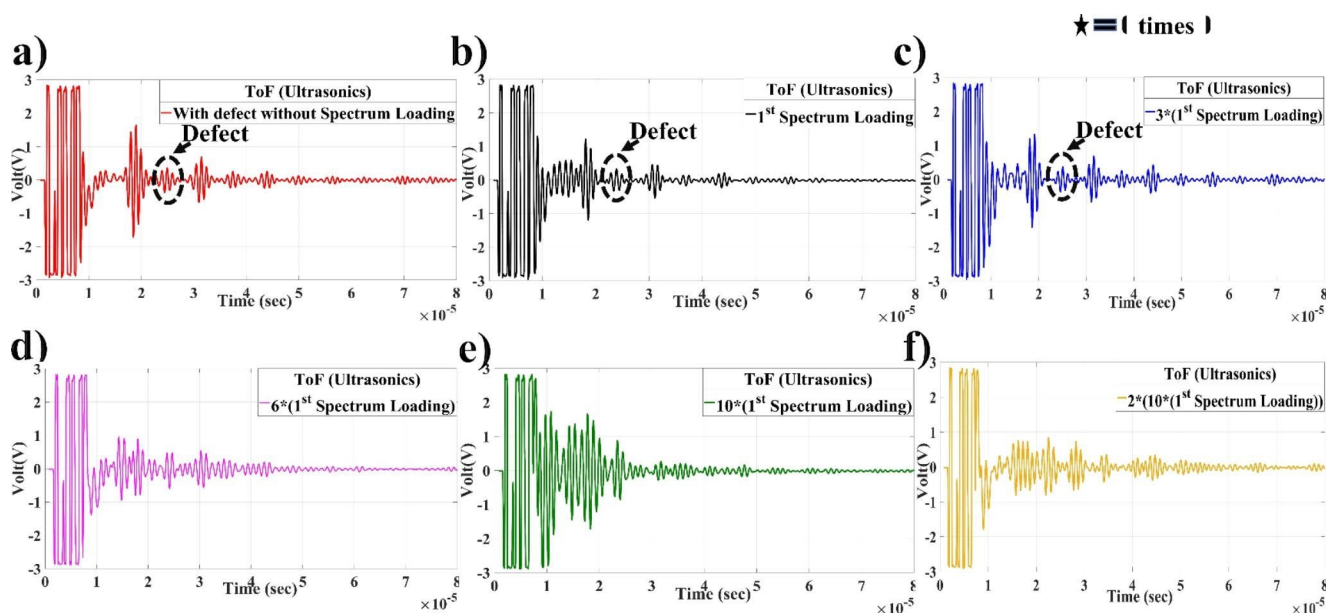


Fig. 11 Time of Flight (ToF) study during each stage of spectrum loading obtained from experiment: **a-c** detection of defects easily trackable by conventional ultrasound ((with defect without spectrum loading, 1st

spectrum loading, 3*(1st spectrum loading)) **d-f** crack defect not easily trackable by conventional ultrasound

scatter more with incoming incident waves and back wall reflection of the specimen. This interference becomes more destructive at 6th spectrum loading, which can be seen at a step time of 6μsec as the back wall reflection becomes denser due to the change in the elliptic nature of the hole. This again becomes denser at 10th spectrum loading. This non-uniformity in the interference of incident waves makes the difference in time-shifting between incident waves and reflection from the crack.

As seen in Fig. 10e, the incident waves interacted first with the crack tip end, which protruded out triangularly with a dimension of 4.774 mm from the centre of the hole, as can be seen from the optical image of Fig. 5e. These ultrasonic incident waves passed through the crack tip, propagated to the elliptic hole bulging out in the direction of loading, and then returned to the crack tip. This wave propagation caused more destructive interference with the incoming waves and scattered from the hole’s elliptic portion and the triangular crack tip end. As seen in Fig. 11, ToF is plotted to monitor the location and growth of crack propagation at each stage of spectrum loading. At every stage of crack propagation, the dimension of crack propagation varies with the application of tensile and compressive loading, as explained in Fig. 5a-e. As observed from the ToF graph, for a specimen with a defect before spectrum fatigue loading, the time difference between the first reflection from the transducer probe and the reflection from the hole is 5.95 μsec which is for a hole dimension of 2.626 mm. When the 1st spectrum loading is applied to the specimen, the time difference is observed as 5.8μsec and again changed to 5.95 μsec for the

3rd spectrum. It is because of the time interval taken from the first reflection from the transducer to the crack region. Here, the minor axis decreased its dimension during each stage of spectrum loading, and the central axis increased its dimension. So, sizes varied with the repeated action of tension and compression, as explained in Fig. 8. But after the 10th spectrum loading, the dimensions changed like a nonlinear pattern at the minor axis increased as observed from the optical macroscope. So, the time difference from the 1st reflection of the probe to crack length is not detectable, as observed from the ToF graphs of Fig. 11d-f. So, the crack monitoring potential by the ultrasonic ToF method is not capable enough to confirm the crack growth in the post-processing technique. Also, during fatigue spectrum loading, it did not sense the crack growth because it’s an advanced NDT method only for post-processing analysis. So, graphene nanoplatelets helped a lot in sensing the crack growth with baseline shifting during piezoresistive action. It helps during spectrum fatigue, where loss can be avoided during mechanical failure [42–45].

5 Conclusion

This paper focused on investigating the crack on a hole-assisted SS304 specimen by a smart graphene doped PMMA sensor and ultrasound technique. The defected SS304 specimen dissipated energy through the hole during crack propagation in spectrum fatigue loading. This has got the function of spectrum fatigue loading at 1st spectrum loading

amplitudes of 0.1 mm, 0.2 mm, 0.3 mm, 0.4 mm, 0.5 mm, 0.4 mm, 0.3 mm, 0.2 mm, and 0.1 mm. The crack at the initial stage was 2.62 mm at both the major and minor axis. But after crossing the 2nd spectrum loading by increasing amplitude three times, the 3rd spectrum loading with an increment of amplitude 6*times, and the 4th spectrum loading with an increment of amplitude 10*times, the crack increased to 2.763 mm, 3.19 mm, and 3.45 mm at the major axis. While failure occurred at the 5th spectrum loading, that is, at 2*10*(1st spectrum loading), the dimension of the hole extended to 4.774 mm at the major and 6.620 mm at the minor axis zone. The change in electrical resistance increased with the growth of the crack. So, the resistance was increased to 14 Ω , 32 Ω , 44 Ω and 106 Ω for the 1st spectrum load, 3*(1st spectrum loading), 6*(1st spectrum loading) and 10*(1st spectrum loading), respectively. During failure at 2*10*(1st spectrum loading), the resistance fell to 88 Ω due to the dissipation of energy through the crack. This experimental crack study was also nicely correlated with FEM simulation by ABAQUS software. The time of flight approach in NDT is a post-processing approach in crack monitoring where it was found difficult to spot the crack location after 3*(1st spectrum loading). Hence, crack monitoring by GNPs sensors helps detect crack growth compared to the advanced conventional ultrasound NDT approach.

Authors' Contributions All authors contributed to the study conception and design. Material preparation, data collection, and analysis were performed by [Debadatta Sethy]. Experimental support provided by [Krishnan Balasubramaniam] and [Sandeep Kumar S R]. The first draft of the manuscript was written by [Debadatta Sethy] and all authors commented on previous versions of the manuscript. Conceptualization, review, and editing were done by [Krishnan Balasubramaniam]. All authors read and approved the final manuscript.

Funding Acknowledgement This research did not receive any specific grant from funding agencies in the public, commercial, or not-for-profit sector. No funding was received to assist with the preparation of this manuscript.

Data Availability The datasets generated during and/or analyzed during the current study are available from the corresponding author on reasonable request.

Declarations

Conflict of Interest The authors declare that they have no known competing financial interests or personal relationships that could have appeared to influence the work reported in this paper.

References

- Sethy, D., Balasubramaniam, K.: Graphene nanoplatelet (GNP)-doped poly (methyl methacrylate) (PMMA) spray-coated piezoresistive-based 2D strain sensor under temperature environment on aluminium alloy 2024-T351. *J Nanopart Res* 24, 118 <https://doi.org/10.1007/s11051-022-05504-5> (2022)
- Niyogi, S., Bekyarova, E., Itkis, M.E., McWilliams, J.L., Hamon, M.A., Haddon, R.C.: Solution Properties of Graphite and Graphene. *J. Am. Chem. Soc* 128, 24, 7720–7721 <https://doi.org/10.1021/ja060680r> (2006)
- Sethy, D., Balasubramaniam, K.: Smart Graphene Nanoplatelet Strain Sensor for Natural Frequency Sensing of Stainless Steel (SS304) and Human Health Monitoring. *Materials* 2022, 15, 3924. <https://doi.org/10.3390/ma15113924>
- Adams, T.M., Layton, R.A.: Piezoresistive transducers. In: Adams, T.M., Layton, R.A. (eds.) *Introductory MEMS: Fabrication and Applications*. Springer US (2010)
- Sethy, D., Makireddi, S., Varghese, F.V., Balasubramaniam, K.: Piezoresistive behaviour of graphene nanoplatelet (GNP)/PMMA spray coated sensors on a polymer matrix composite beam. *eXPRESS Polymer Letters* 13,1018–1025 <https://doi.org/10.3144/expresspolymlett.2019.88> (2019)
- Ganguli, S., Roy, A.K., Anderson, D.P.: Improved thermal conductivity for chemically functionalized exfoliated graphite/epoxy composites. *Carbon* 46, 806–817 <https://doi.org/10.1016/j.carbon.2008.02.008> (2008)
- Sethy, D., Makireddi, S., Varghese, F.V., Balasubramaniam, K.: Improved Thermal Signature of Composite Beams with GNP Smart Skin for Defect Investigation. *Journal of Nondestructive Evaluation* 80, 1–14 <https://doi.org/10.1007/s10921-021-00817-2> (2021)
- Wang, Y., Qiu, L., Luo, Y., Ding, R.: A stretchable and large-scale guided wave sensor network for aircraft smart skin of structural health monitoring. *Structural Health Monitoring*. ;20(3):861–876. <https://doi.org/10.1177/1475921719850641> (2021)
- Wang, Y., Qiu, L., Luo, Y., Ding, R., Jiang, F.: A piezoelectric sensor network with shared signal transmission wires for structural health monitoring of aircraft smart skin. *Mechanical systems and Signal Processing* 141 106730. <https://doi.org/10.1016/j.ymssp.2020.106730> (2020)
- Aram, E., Ehsani, M., Khonakdar, H.A., Abdollahi, S.: Improvement of electrical, thermal, and mechanical properties of poly (methyl methacrylate)/poly (ethylene oxide) blend using graphene nanosheets. *Journal-of-Thermoplastic-Composite-Materials* 32, 1176–1189 <https://doi.org/10.1177/0892705718794776> (2018)
- Yang, J., Qi, G.Q., Liu, Y., Bao, R.Y., Liu, Z.Y., Yang, W., Lie, B.H., Yang, M.B.: Hybrid graphene aerogels/phase change material composites: thermal conductivity, shape-stabilization and light-to-thermal energy storage. *Carbon* 100, 693–702 <https://doi.org/10.1016/j.carbon.2016.01.063> (2016)
- Wu, H., Lu, C., Zhang, W., Zhang, X.: Preparation of low-density polyethylene/low-temperature expandable graphite composites with high thermal conductivity by an in-situ expansion melt blending process. *Mater. Des* 52, 621–629 <https://doi.org/10.1016/j.matdes.2013.05.056> (2013)
- Guo, H., Li, X., Li, B., Wang, J., Wang, S.: Thermal conductivity of graphene/poly (vinylidene fluoride) nanocomposite membrane. *Mater. Des* 114, 355–363 <https://doi.org/10.1016/j.matdes.2016.11.010> (2017)
- Kim, S.Y., Ye, J.N., Yu, J.: Thermal conductivity of graphene nanoplatelets filled composites fabricated by solvent-free processing for the excellent filler dispersion and a theoretical approach for the composites containing the geometrized fillers. *Compos. Part A* 69, 219–225 <https://doi.org/10.1016/j.compositesa.2014.11.018> (2015)
- Hazarika, M., Jana, T.: Graphene nanosheets generated from sulfonated polystyrene/graphene nanocomposite. *Compos. Sci. Technol* 87, 94–102 <https://doi.org/10.1016/j.compotech.2013.08.004> (2013)

16. Li, X., Linbo, S., Song, N., Shi, L., Ding, P.: Enhanced thermal conductive and anti-dripping properties of polyamide composites by 3D graphene structures at low filler content. *Compos. Part A* **88**, 305–314 <https://doi.org/10.1016/j.compositesa.2016.06.007> (2016)
17. Tsai, M.W., Chuang, T.H., Meng, C.Y., Chang, Y.T., Lee, S.C.: High performance mid infrared narrow-band plasmonic thermal emitter. *Appl. Phys. Lett* **89**, 173116 <https://doi.org/10.1063/1.2364860> (2006)
18. Mahmoud, E., Al-Bluwi, S.A.: Development of ultrasensitive mechanical strain sensor made of 2D-assembled graphene monolayers aligned parallel into polysilicon nanocomposites. *Sensors and Actuators A: Physical* **313**, 112166 (2020). <https://doi.org/10.1016/j.sna.2020.112166>
19. Njuguna, M.K., Yan, C., Hu, N., Bell, J.M., Yarlagadda, P.K.D.V.: Sandwiched carbon nanotube film as strain sensor. *Composites Part B: Engineering* **43**, 2711–2717 (2012). <https://doi.org/10.1016/j.compositesb.2012.04.022>
20. Mehmood, A., Mujawar, M.N., Khalid, M.W.R., Abdullah, E.C., Siddiqui, M.T.H., Baloch, H., Sabzoi, N., Mazari, S.: Graphene based nanomaterials for strain sensor application—a review. *Journal-of-Environmental-Chemical-Engineering* **8**, 103743 <https://doi.org/10.1016/j.jece.2020.103743> (2020)
21. Liu, H., Gao, H., Hu, G.: Highly sensitive natural rubber/pristine graphene strain sensor prepared by a simple method. *Composites Part B* **171**, 138–145 (2019). <https://doi.org/10.1016/j.compositesb.2019.04.032>
22. Yu, R., Zhu, C., Wan, J., Li, Y., Hong, X.: Review of Graphene-Based Textile Strain Sensors, with Emphasis on Structure Activity Relationship. *Polymers MDPI* **13**(1), 151 <https://doi.org/10.3390/polym13010151> (2021)
23. Maurya, D., Khaleghian, S., Sriramdas, R., Kumar, P., Kishore, R.A., Kang, M.G., Kumar, V., Song, H.C., Lee, S.Y., Yan, Y., Park, J.M., Taheri, S., Priya, S.: 3D printed graphene-based self-powered strain sensors for smart tires in autonomous vehicles. *Nature communications* **11**, 5392 <https://doi.org/10.1038/s41467-020-19088-y> (2020)
24. Lecomte, C., Graham, W.R., Dale, M.A.: A shell model for tyre belt vibrations. *J. Sound Vib* **329**, 1717–1742 <https://doi.org/10.1016/j.jsv.2009.11.022> (2010)
25. Morinaga, H., Wakao, Y., Hanatsuka, Y., Kobayakawa, A.: The possibility of intelligent tire (Technology of Contact Area Information Sensing). In: *Proc. FISITA Trans. (F2006V104) World Automotive Congress* (2006)
26. Keoh, S.L., Kumar, S.S., Tschofenig, H.: Securing the internet of things: a standardization perspective. *IEEE Internet Things J* **1**, 265–275 <https://doi.org/10.1109/JIOT.2014.2323395> (2014)
27. Pei, W., Zhang, T., Wang, Y., Chen, Z., Umar, A., Li, H., Guo, W.: Enhancement of charge transfer between graphene and donor – acceptor molecule for ultrahigh sensing performance. *Nanoscale* **9**, 16273–16280 <https://doi.org/10.1039/C7NR04209D> (2017)
28. Marcano, D.C., Kosynkin, D.V., Berlin, J.M., Sinititskii, A., Sun, Z., Slesarev, A., Alemany, L.B., Lu, W., Tour, J.M.: Improved synthesis of graphene oxide. *ACS Nano* **4**, 8, 4806–4814 <https://doi.org/10.1021/nn1006368> (2010)
29. Carvajal, N.A., Mayer, A.L.: Functionalized Graphene Surfaces for Selective Gas Sensing. *ACS Omega* **5**, 34, 21320–21329 <https://doi.org/10.1021/acsomega.0c02861> (2020)
30. Tiwari, D.C., Atri, P., Sharma, R.: Sensitive detection of ammonia by reduced graphene oxide/polypyrrole nanocomposites. *Synth. Met* **203**, 228–234 <https://doi.org/10.1016/j.synthmet.2015.02.026> (2015)
31. Tang, X., Raskin, J.P., Kryvutsa, N., Hermans, S., Slobodian, O.M., Nazarov, A.N., Debliquy, M.: An ammonia sensor composed of polypyrrole synthesized on reduced graphene oxide by electropolymerization. *Sensors-and-Actuators-B-Chemical* **305**, 127423 <https://doi.org/10.1016/j.snb.2019.127423> (2019)
32. Jia, R., Xie, P., Feng, Y., Chen, Z., Umar, A., Wang, Y.: Dipole modified graphene with ultrahigh gas sensibility. *Appl. Surf. Sci* **440**, 409–414 <https://doi.org/10.1016/j.apsusc.2018.01.166> (2018)
33. Parks, V.J., Durelli, A.J.: Various forms of the strain-displacement relations applied to experimental strain analysis. *Exp. Mech* **4**, 37–47 <https://doi.org/10.1007/BF02323962> (1964)
34. Makireddi, S., Sethy, D., Varghese, F.V., Balasubramaniam, K.: Cyclic loading behaviour and crack monitoring potential of graphene nanoplatelet (GNP) based strain sensors in simple structures. *Mater. Res. Express* **5**, 035701(). <https://doi.org/10.1088/2053-1591/aaaf7b> (2018)
35. Huang, Y., Xiang, Y., Ren, W.T., Li, F., Li, C., Yang, T.T.: Enhancing the sensitivity of crack-based strain sensor assembled by functionalized graphene for human motion detection. *Science China Technological Sciences* **64**, 1805–1813 <https://doi.org/10.1007/s11431-021-1856-6> (2021)
36. Liao, X., Zhang, Z., Liao, Q., Liang, O., Ou, Y., Xu, M., Li, M., Zhang, G., Zhang, Y.: Flexible and printable paper-based strain sensors for wearable and large-area green electronics. *Nanoscale* **8**, 13025–13032 <https://doi.org/10.1039/C6NR02172G> (2016)
37. Song, H., Zhang, J., Chen, D., Wang, K., Niu, S., Han, Z., Ren, L.: Superfast and high-sensitivity printable strain sensors with bioinspired micron-scale cracks. *Nanoscale* **9**, 1166–1173 <https://doi.org/10.1039/C6NR07333F> (2017)
38. Caputo, F., Lamanna, G., Soprano, A.: On the evaluation of the plastic zone size at the crack tip. *Eng. Fract. Mech.* **103** 162–173. <https://doi.org/10.1016/j.engfracmech.2012.09.030> (2013)
39. Mao, L., Gong, T., Ai, Q., Hong, Y., Guo, J., He, Y., Huang, W., Yu, B.: Morphologically modulated laser-patterned reduced graphene oxide strain sensors for human fatigue recognition. *Smart Mater. Struct* **29**, 015009 (<https://doi.org/10.1088/1361-665X/ab52c0>) (2020)
40. Young, W.C., Budynas, R.G.: *Roark's Formulas for Stress and Strain*. McGraw-Hill, New York 7th Edition, ISBN 0-07-072542-X, (2002)
41. Gairola, S., Jayaganthan, R.: XFEM Simulation of Tensile and Fracture Behavior of Ultrafine-Grained Al 6061 Alloy. *Metals MDPI* **11**(11), 1761 <https://doi.org/10.3390/met11111761> (2021)
42. Shedbale, A., Sharma, A.K., Singh, I.V., Mishra, B.K.: Modeling and Simulation of Metal Forming Processes by XFEM. *Applied-Mechanics-and-Materials* **829**, 41–45 <https://doi.org/10.4028/www.scientific.net/AMM.829.41> (2016)
43. Talemi, R.H., Cooreman, S., Hoecke, D.V.: Finite element simulation of dynamic brittle fracture in pipeline steel: A XFEM-based cohesive zone approach. *Journal of Materials: Design and Applications* **232**(5), 357–370. <https://doi.org/10.1177/1464420715627379>
44. Fuan, S.I., Ke, M.A., Kanghe, L., Kun, L.I., Aliha, M.R.M.: Influence of specimen geometry on mode I fracture toughness of asphalt concrete. *Constr. Build. Mater.* **276** 122181. <https://doi.org/10.1016/j.conbuildmat.2020.122181> (2021)
45. Anderson TL, “Fracture Mechanics: Fundamentals and Applications,” 3rd Edition

Publisher's Note Springer Nature remains neutral with regard to jurisdictional claims in published maps and institutional affiliations.

Springer Nature or its licensor holds exclusive rights to this article under a publishing agreement with the author(s) or other rightsholder(s); author self-archiving of the accepted manuscript version of this article is solely governed by the terms of such publishing agreement and applicable law.